

ORIGINAL ARTICLE

Open Access



Effect of Dynamic Pressure Feedback Orifice on Stability of Cartridge-Type Hydraulic Pilot-Operated Relief Valve

Yaobao Yin^{1*}, Dong Wang¹ , Junyong Fu² and Hong-chao Jian³

Abstract

Current research on pilot-operated relief valve stability is primarily conducted from the perspective of system dynamics or stability criteria, and most of the existing conclusions focus on the spool shape, damping hole size, and pulsation frequency of the pump. However, the essential factors pertaining to the unstable vibration of relief valves remain ambiguous. In this study, the dynamic behavior of a pilot-operated relief valve is investigated using the frequency-domain method. The result suggests that the dynamic pressure feedback orifice is vital to the dynamic characteristics of the valve. A large orifice has a low flow resistance. In this case, the fluid in the main spring chamber flows freely, which is not conducive to the stability of the relief valve. However, a small orifice may create significant flow resistance, thus restricting fluid flow. In this case, the oil inside the main valve spring chamber is equivalent to a high-stiffness liquid spring. The main mass-spring vibration system has a natural frequency that differs significantly from the operating frequency of the relief valve, which is conducive to the stability of the relief valve. Good agreement is obtained between the theoretical analysis and experiments. The results indicate that designing a dynamic pressure feedback orifice of an appropriate size is beneficial to improving the stability of hydraulic pilot-operated relief valves. In addition, the dynamic pressure feedback orifice reduces the response speed of the relief valve. This study comprehensively considers the stability, rapidity, and immunity of relief valves and expands current investigations into the dynamic characteristics of relief valves from the perspective of classical control theory, thus revealing the importance of different parameters.

Keywords Pilot-operated relief valve, Dynamic pressure feedback orifice, Stability, Rapidity, Immunity

1 Introduction

To guarantee a smooth and accurate performance of the actuator, hydraulic systems are typically designed to operate within a specified pressure range. Relief valves are frequently used in hydraulic systems to limit the maximum pressure in a system or to prevent hydraulic circuits from

overloading [1]. In general, relief valves can be categorized into direct and pilot types. The pilot type is a two-stage structure invented by Vickers in 1931 [2]. Owing to their effective pressure control properties, pilot-operated relief valves are used extensively in hydraulic control systems featuring high pressures and large flows. However, during operation, relief valves occasionally vibrate, thus causing system pressure fluctuations and severely reducing the safety, stability, and reliability of the hydraulic system [3].

Several analyses from various perspectives have been performed to clarify the instability and vibration of relief valves. One approach is to conduct various studies to determine the causes of instability. Hayashi investigated

*Correspondence:

Yaobao Yin

y-yin@tongji.edu.cn

¹ School of Mechanical Engineering, Tongji University, Shanghai 201804, China

² Shanghai Aerospace Control Technology Institute, Shanghai 201109, China

³ China North Vehicle research institute, Beijing 100072, China



© The Author(s) 2023. **Open Access** This article is licensed under a Creative Commons Attribution 4.0 International License, which permits use, sharing, adaptation, distribution and reproduction in any medium or format, as long as you give appropriate credit to the original author(s) and the source, provide a link to the Creative Commons licence, and indicate if changes were made. The images or other third party material in this article are included in the article's Creative Commons licence, unless indicated otherwise in a credit line to the material. If material is not included in the article's Creative Commons licence and your intended use is not permitted by statutory regulation or exceeds the permitted use, you will need to obtain permission directly from the copyright holder. To view a copy of this licence, visit <http://creativecommons.org/licenses/by/4.0/>.

the stability of single-stage poppet valves, and the results indicated that various factors, such as the effects of the valve poppet and seat, and the hysteresis of the transient hydrodynamic force, might cause the poppet valve to destabilize vibrations [4]. Additionally, some studies indicate that the stability of relief valves can be affected by the pre-compression shrinkage of springs [5], half cone angle [6], damping orifice size [7], flow rate in valve chambers [8], spool damping coefficient [9], valve orifice diameter [10], upstream and downstream pipelines [11, 12], cavitation [13–16], impact between the spool and seat [17], and valve chamber volume [18]. In addition, some scholars established a fluid–structure interaction model of the relief valve and investigated its stability [19, 20]. Meanwhile, some scholars investigated the effects of various parameters on the stability of the valve via theoretical analysis and simulations [21–23], whereas others have experimentally obtained the conditions for the steady operation of the relief valve [24].

Numerous strategies have been proposed to increase the stability of relief valves. Merrit placed a fixed office between a pressure-controlled chamber and valve port and discovered that reasonably matching the fixed office with the sensitive chamber volume can increase the relief valve stability [25]. Moreover, designing a buffer structure at the end of the valve poppet can enhance its stability [26].

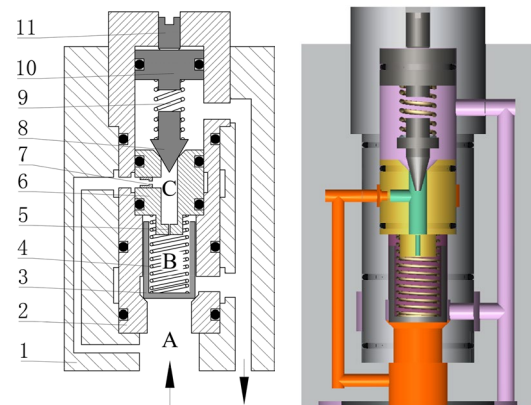
Although the stability of relief valves has been investigated extensively, quantitative agreement between predicted and measured stabilities has not been achieved because parameters such as damping and friction coefficients cannot be easily calculated accurately; therefore, the orifice size can only be confirmed through extensive experiments. However, because hydraulic technology is developing toward miniaturization, intelligence, and high performance, the relevant theories must be supplemented urgently.

In this study, the stability of a cartridge-type pilot-operated relief valve is investigated via frequency-domain analysis. In addition, a Bode diagram is used to assess elements that are different between the original and contrast models. Finally, theoretical conclusions are presented based on numerical simulation and experimental results.

2 Mathematical Model of Pilot-operated Relief Valve

2.1 Description of Pilot-operated Relief Valve

Generally, a pilot-operated relief valve comprises a main valve and a pilot valve. Figure 1 shows the structural diagram of a cartridge-type antivibration pilot-operated relief valve, and its schematic diagram is illustrated in Figure 2. The system pressure p_s is transmitted to the sensitive chamber C through the sharp-edged orifice



1. valve block; 2. valve sleeve; 3. main poppet; 4. main spring; 5. dynamic pressure feedback orifice R_2 ; 6. pilot valve seat (main spring seat); 7. thin wall orifice R_1 ; 8. pilot poppet; 9. pilot spring; 10. pilot spring seat; 11. adjustment bolt; A. Pressure controlled chamber; B. Pressure sensing chamber; C. Pressure sensitive chamber.

Figure 1 Structure diagram of pilot-operated relief valve

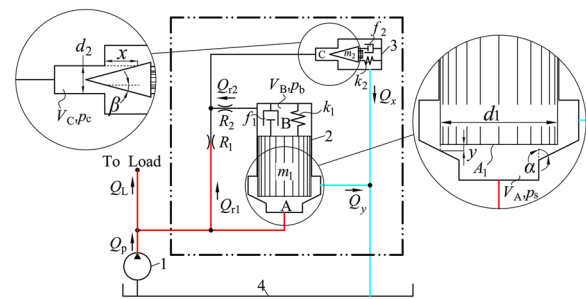


Figure 2 Schematic diagram of pilot-operated relief valve

R_1 and then transmitted to the pressure-sensing chamber B through the dynamic pressure feedback orifice R_2 , which is sensed by the pilot valve. If p_s does not exceed the cracking pressure, then the pilot valve is closed by the preload spring force. Based on Pascal's law, $p_s = p_b = p_c$; thus, the main poppet is hydraulically balanced. However, it is also maintained in the seat by a pre-loaded spring force. Any positive deviation from the reference value causes the pilot port to open and flow, thus causing the main poppet to be unbalanced due to the pressure difference Δp between chambers A and B. Consequently, the main poppet is lifted and relieves the system flow from chamber A to the tank.

The following assumptions were introduced to derive a mathematical model for the relief valve:

1. The bulk modulus of the fluid is constant.

2. The valve outlet pressure is equal to the tank pressure.
3. Perturbations are minimal, which allows the mathematical model to be linearized at the rated operating point.
4. Leakage around the main poppet is negligible.

2.2 Static Characteristics

Under steady state, the physical model of the pilot-operated relief valve is described as follows:

The steady flow passing through the relief valve is expressed as

$$Q_p - Q_L = Q_x + Q_y, \tag{1}$$

where Q_p is the supply flow rate, Q_L the flow rate to the load, Q_x the flow rate at the pilot port, and Q_y the flow rate at the main port.

The mechanical equilibrium equation of the main poppet is

$$A_1(p_s - p_b) = k_1(y + y_0) + F_{s1}, \tag{2}$$

where A_1 is the cross-sectional area of the main poppet; p_s is the pressure in chamber A; p_b is the pressure in chamber B; k_1 is the main spring stiffness; y is the main valve displacement; and y_0 is the constant pre-compression of the main spring. Meanwhile, F_{s1} is the steady flow force of the main valve, expressed as $F_{s1} = \rho Q_y v_y \cos \alpha = C_{d1} C_{v1} \pi d_1 \sin(2\alpha) y p_s$, where ρ is the fluid density, v_y the main port flow velocity, α the half-angle of the main valve, C_{d1} and C_{v1} are the discharge and velocity coefficients of the main exit port, respectively, and d_1 the diameter of the main exit port.

The flow rate passing through the main exit port can be represented by the following well-established relationship:

$$Q_y = C_{d1} A_y \sqrt{\frac{2p_s}{\rho}}, \tag{3}$$

where A_y denotes the cross-sectional area of the main port. Here, $A_y = \pi d_1 y \sin \alpha \left(1 - \frac{y}{2d_1} \sin 2\alpha\right)$, and because $y \ll d_1$, A_y can be approximated as $A_y = \pi d_1 y \sin \alpha$.

The flow rate passing through the sharp-edged orifice R_1 is expressed as

$$Q_{r1} = C_{r1} \frac{\pi d_{r1}^2}{4} \sqrt{\frac{2(p_s - p_c)}{\rho}}, \tag{4}$$

where C_{r1} is the discharge coefficient of orifice R_1 , d_{r1} the diameter of orifice R_1 , and p_c the pressure in chamber C.

The mechanical equilibrium equation of the pilot poppet is

$$A_2 p_c = k_2(x + x_0) + F_{s2}, \tag{5}$$

where A_2 is the cross-sectional area of the pilot poppet, k_2 the pilot spring stiffness, x the pilot valve displacement, and x_0 the pre-compression constant of the pilot spring. F_{s2} is the steady flow force of pilot valve, expressed as $F_{s2} = \rho Q_x v_x \cos \beta = C_{d2} C_{v2} \pi d_2 \sin(2\beta) x p_b$, where v_x is the pilot port flow velocity, β the half-angle of the pilot poppet, C_{d2} and C_{v2} are the discharge coefficient and velocity coefficient of pilot port, respectively, and d_2 is the diameter of the pilot port.

The flow rate passing through the dynamic pressure feedback orifice R_2 is expressed as

$$Q_{r2} = \frac{\pi d_{r2}^4}{128 \mu l_{r2}} (p_b - p_c), \tag{6}$$

where d_{r2} and l_{r2} are the diameter and length of orifice R_2 , respectively; μ is the dynamic viscosity of the fluid; and $p_b = p_c$ in steady state.

The flow rate passing through the pilot port is expressed as

$$Q_x = C_{d2} A_x \sqrt{\frac{2p_c}{\rho}}, \tag{7}$$

where A_x is the cross-sectional area of the pilot port. Here, $A_x = \pi d_2 x \sin \beta \left(1 - \frac{x}{2d_2} \sin 2\beta\right)$, and because $x \ll d_2$, A_x can be approximated as $A_x = \pi d_2 x \sin \beta$.

2.3 Dynamic Mathematical Model

In the transient state, the mathematical model of the pilot-operated relief valve is as follows:

As shown in Figure 2, the continuity equation applied to chamber A of volume V_A yields

$$Q_p - Q_L - Q_{r1} - Q_y - \frac{V_A}{E} \frac{dp_s}{dt} - A_1 \frac{dy}{dt} = 0, \tag{8}$$

where E is the bulk stiffness of the fluid.

The mechanical equilibrium equation of the main poppet is

$$m_1 \frac{d^2 y}{dt^2} = A_1(p_s - p_b) - k_1(y + y_0) - F_{s1} - f_1 \frac{dy}{dt}, \tag{9}$$

where m_1 is the effective main poppet mass (including 1/3 of the spring mass); and f_1 is the viscous damping coefficient of the main poppet, which is expressed as

$$f_1 = f_{m1} + f_{t1}, \tag{10}$$

where, f_{m1} and f_{t1} are expressed as

$$f_{m1} = \frac{\mu A_m}{\delta_1}, \tag{11}$$

$$f_{t1} = C_{d1} \pi d_1 l_1 \sin(\alpha) \sqrt{2\rho p_s}, \tag{12}$$

where, A_m is the equivalent wetting area of the main poppet; δ_1 the clearance between the main poppet and valve body; and l_1 the damping length of the main poppet.

The flow continuity equation applied to chamber B of volume V_B can be written as

$$A_1 \frac{dy}{dt} - Q_{r2} - \frac{V_B}{E} \frac{dp_b}{dt} = 0. \tag{13}$$

The continuity equation applied to chamber C of volume V_C yields

$$Q_{r1} + Q_{r2} - Q_x - A_2 \frac{dx}{dt} - \frac{V_C}{E} \frac{dp_c}{dt} = 0. \tag{14}$$

The mechanical equilibrium equation of the pilot poppet is

$$m_2 \frac{d^2x}{dt^2} = A_2 p_c - k_2(x + x_0) - F_{s2} - f_2 \frac{dx}{dt}, \tag{15}$$

where m_2 is the effective pilot poppet mass (including 1/3 of the spring mass); and f_2 is the viscous damping coefficient of the pilot poppet, which is expressed as

$$f_2 = f_{m2} + f_{t2}, \tag{16}$$

where f_{m2} and f_{t2} are expressed as

$$f_{m2} = \mu \frac{A_p}{\delta_2}, \tag{17}$$

$$f_{t2} = C_{d2} \pi d_2 l_2 \sin(\beta) \sqrt{2\rho p_c}, \tag{18}$$

where, A_p is the equivalent wetting area of the pilot poppet, δ_2 the clearance between the pilot poppet and valve body, and l_2 the damping length of the pilot poppet.

2.4 Linearization Analysis

Directly analyzing a higher-order complex system using classical control theory is challenging. Linearization is a widely used mathematical approach in mechanical engineering. Consider a slight perturbation near the rated operating point. Subsequently, using the Laplace

transform of Eqs. (3), (4), (6)–(9), and (13)–(15), the following mathematical model can be obtained:

$$Q_y = K_A p_s + K_B y, \tag{19}$$

$$Q_{r1} = K_C(p_s - p_c), \tag{20}$$

$$Q_{r2} = G_r(p_b - p_c), \tag{21}$$

$$Q_x = K_E p_c + K_F x, \tag{22}$$

$$Q_p - Q_L - Q_y - Q_{r1} - \frac{V_A}{E} p_{s'} - A_1 y_s = 0, \tag{23}$$

$$(A_1 - K_D y_x) p_s - A_1 p_b = (m_1 s^2 + f_1 s + k_1 + K_D p_{sx}) y, \tag{24}$$

$$A_1 y_s - Q_{r2} - \frac{V_B}{E} p_b s = 0, \tag{25}$$

$$Q_{r1} + Q_{r2} - Q_x - A_2 x_s - \frac{V_C}{E} p_c s = 0, \tag{26}$$

$$(A_2 - K_G x_x) p_c = (m_2 s^2 + f_2 s + k_2 + K_G p_{cx}) x, \tag{27}$$

where, y_x and x_x are the main and pilot valve displacements under the rated operating point, respectively; and p_{sx} and p_{cx} are the pressures in chambers A and C under the rated operating point, respectively.

The physical meanings and expressions of K_n are shown in Table 1.

3 Contrast Model

To analyze the effect of the dynamic pressure feedback orifice R_2 , a pilot-operated relief valve without a dynamic pressure feedback orifice is proposed as a contrast model, as shown in Figures 3 and 4.

4 Theoretical Analysis

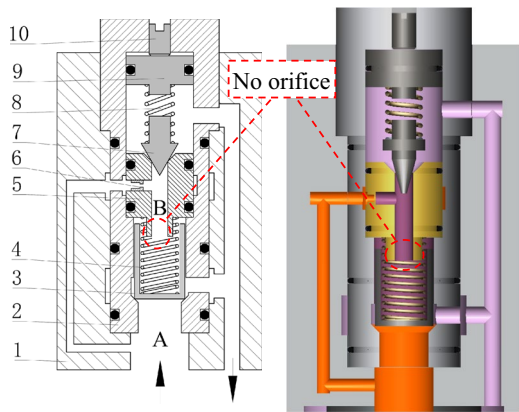
4.1 System Block Diagram

In this section, the effect of the dynamic pressure feedback orifice is analyzed using the frequency-domain method. Using the flow rate at inlet $Q_p - Q_L$ as the input and the pressure of chamber A, p_s , as the output, the system block diagrams of the original and contrast models are developed, as shown in Figures 5 and 6, respectively.

The physical meanings and expressions of ω_n are presented in Table 2. A comparison of Figures 5 and 6

Table 1 Physical meanings and expressions of K_n

Sign	Physical meaning	Expressions
K_A	Pressure-flow coefficient of main exit port.	$K_A = C_{d1} \pi d_1 \sin \alpha y_x \sqrt{\frac{1}{2\rho p_{sx}}}$
K_B	Flow gain of main exit port.	$K_B = C_{d1} \pi d_1 \sin \alpha \sqrt{\frac{2p_{sx}}{\rho}}$
K_C	Hydraulic conductivity of orifice R_1 .	$K_C = \frac{\pi d_{r1}^2}{4} C_{r1} \sqrt{\frac{1}{2\rho(p_{sx}-p_{cx})}}$
K_D	Equivalent stiffness of steady hydrodynamic force of the main valve.	$K_D = C_{d1} C_{v1} \pi d_1 \sin(2\alpha)$
K_E	Pressure-flow coefficient of pilot port.	$K_E = C_{d2} \pi d_2 x_x \sin \beta \sqrt{\frac{1}{2\rho p_{cx}}}$
K_F	Flow gain of pilot port.	$K_F = C_{d2} \pi d_2 \sin \beta \sqrt{\frac{2p_{cx}}{\rho}}$
K_G	Equivalent stiffness of Steady hydrodynamic force of the pilot valve.	$K_G = C_{d2} C_{v2} \pi d_2 \sin(2\beta)$
G_r	Hydraulic conductivity of orifice R_2 .	$G_r = \frac{\pi d_r^2}{128\mu l_2}$



1. valve block; 2. valve sleeve; 3. main poppet; 4. main spring; 5. pilot valve seat; 6. thin wall orifice R_1 ; 7. pilot poppet; 8. pilot spring; 9. pilot spring seat; 10. 11. adjustment bolt

Figure 3 Structure diagram of contrast model

reveals the discrepancies between the original and contrast models. Circuits 1 and 3 contain the same components, which indicate the transfer function of the main valve mass–spring vibration system. Circuit 2 depicts the transfer function of pilot valve pressure control chamber C. Circuits 1, 2, and 3 of the original model have one more first-order inertial element than those of the contrast model. According to the classical control theory, for a system comprising a first-order inertial element and

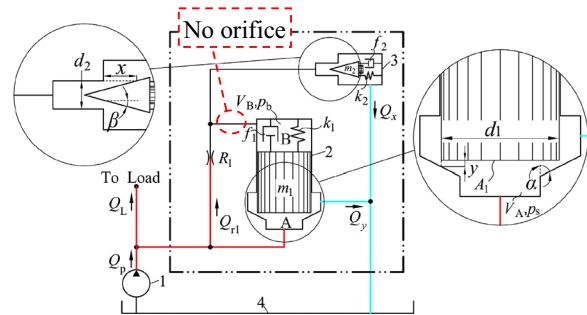


Figure 4 Schematic diagram of contrast model

an oscillation element, the dynamic characteristics are primarily dominated by the first-order inertial element if the break frequency of the first-order inertial element is much lower than that of the oscillation element. The hysteresis of the first-order inertial element can counter-balance the lead effect of the oscillation element, thereby improving the stability of the subsystems. This may be beneficial to the global stability of the pilot-operated relief valve.

The complete list of parameters used in the investigation is presented in Table 3.

Solving Eqs. (1)–(7) allows one to determine the steady-state operating point of the relief valve at a flow rate of 90 L/min, as listed in Table 4.

4.2 Dynamic Characteristics of Pilot Valve Subsystem

For the original model, the system transfer function of the pilot valve subsystem can be expressed as

$$G_{\text{pilot-o}}(s) = \frac{\frac{1}{K_C + K_E}}{\left(\frac{s}{\omega_4} + 1\right)\left(\frac{s}{\omega_7} + 1\right) + \frac{s}{\omega_9(K_C + K_E)}} \times \frac{\frac{K_F(A_2 - K_G x_x)}{K_{m2}} \left(\frac{s}{\omega_6} + 1\right) \left(\frac{s}{\omega_7} + 1\right)}{\frac{s^2}{\omega_2^2} + \frac{2\zeta_2}{\omega_2} s + 1}, \quad (28)$$

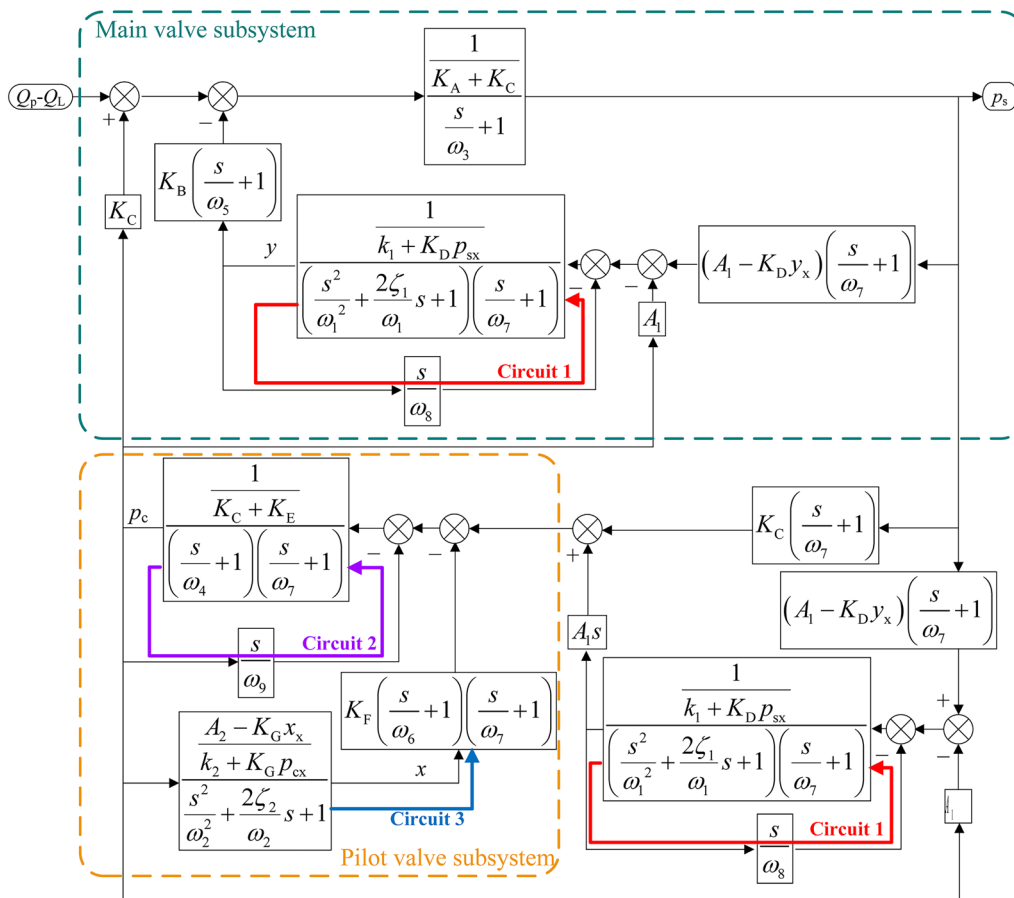


Figure 5 System block diagram of original model

where K_{m2} is the equivalent mechanical spring stiffness of the main valve and $K_{m2} = k_2 + K_G p_{cx}$. Because $V_B \gg V_C$, $\omega_4 \gg \omega_7$, Eq. (28) can be approximated using Eq. (29).

$$G_{pilot-o}(s) = \frac{\frac{K_F(A_2 - K_G x_x)}{K_{m2}(K_C + K_E)} \left(\frac{s}{\omega_6} + 1\right) \left(\frac{s}{\omega_7} + 1\right)}{\left[\left(\frac{s}{\omega_4} + 1\right) \left(\frac{s}{\omega_7} + 1\right) + \frac{s}{\omega_9(K_C + K_E)}\right] \left(\frac{s^2}{\omega_2^2} + \frac{2\zeta_2 s}{\omega_2} + 1\right)}$$

$$\Downarrow$$

$$G_{pilot-o}(s) = \frac{\frac{K_F(A_2 - K_G x_x)}{K_{m2}(K_C + K_E)} \left(\frac{s}{\omega_6} + 1\right) \left(\frac{s}{\omega_7} + 1\right)}{\left[\left(\frac{s}{\omega_7} + 1\right) + \frac{s}{\omega_9(K_C + K_E)}\right] \left(\frac{s^2}{\omega_2^2} + \frac{2\zeta_2 s}{\omega_2} + 1\right)}$$

$$\Downarrow$$

$$G_{pilot-o}(s) = \frac{\frac{K_F(A_2 - K_G x_x)}{K_{m2}(K_C + K_E)} \left(\frac{s}{\omega_6} + 1\right) \left(\frac{s}{\omega_7} + 1\right)}{\left[\left(\frac{V_B}{EG_r} + \frac{V_B}{E(K_C + K_E)}\right) s + 1\right] \left(\frac{s^2}{\omega_2^2} + \frac{2\zeta_2 s}{\omega_2} + 1\right)}$$

$$\Downarrow$$

$$G_{pilot-o}(s) = \frac{\frac{K_F(A_2 - K_G x_x)}{K_{m2}(K_C + K_E)} \left(\frac{s}{\omega_6} + 1\right) \left(\frac{s}{\omega_7} + 1\right)}{\left[\left(\frac{V_B(K_C + K_E) + G_r V_B}{EG_r(K_C + K_E)}\right) s + 1\right] \left(\frac{s^2}{\omega_2^2} + \frac{2\zeta_2 s}{\omega_2} + 1\right)}$$

$$\Downarrow$$

$$G_{pilot-o}(s) = \frac{\frac{K_F(A_2 - K_G x_x)}{K_{m2}(K_C + K_E)} \left(\frac{s}{\omega_6} + 1\right) \left(\frac{s}{\omega_7} + 1\right)}{\left(\frac{s}{\omega_a} + 1\right) \left(\frac{s^2}{\omega_2^2} + \frac{2\zeta_2 s}{\omega_2} + 1\right)}, \quad (29)$$

Table 3 Main parameters used in current study

Parameter	Value	Parameter	Value
m_1 (g)	30.0	δ_1 (μm)	10.0
m_2 (g)	3.5	δ_2 (μm)	20.0
k_1 (N/mm)	20	V_A (mL)	1500
k_2 (N/mm)	40	V_B (mL)	1.905
x_0 (mm)	3.4	V_C (mL)	0.388
y_0 (mm)	5.8	C_{d1}, C_{d2}	0.65
d_1 (mm)	14.0	C_{v1}, C_{v2}	0.98
d_2 (mm)	3.0	E (MPa)	800
α ($^\circ$)	30	ρ (kg/m^3)	833
β ($^\circ$)	15	μ (Pa·s)	1.96e-3
A_m (mm^2)	220	l_1 (mm)	25.0
A_p (mm^2)	94.2	l_2 (mm)	10.0
d_{r1} (mm)	1.0	d_{r2} (mm)	0.8
C_{r1}	0.61	l_{r2} (mm)	10.0

Table 4 Steady-state operating point

Parameter	Value	Parameter	Value
P_{sx} (MPa)	23.0	x_x (mm)	0.10
p_{cx} (MPa)	20.5	y_x (mm)	0.45

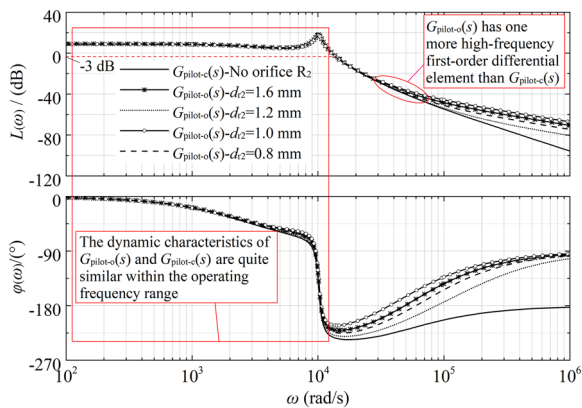


Figure 7 Bode diagrams of $G_{\text{pilot-o}}(s)$ and $G_{\text{pilot-c}}(s)$

$$\omega_a = \frac{EG_r(K_C + K_E)}{V_B(G_r + K_C + K_E)} \quad (30)$$

where ω_a is the break frequency of the first-order inertial element related to orifice R_2 as well as chambers B and C in the original model.

For the contrast model, the system transfer function of the pilot valve subsystem can be expressed as follows:

$$G_{\text{pilot-c}}(s) = \frac{\frac{K_F(A_2 - K_G x_x)}{K_{m2}(K_C + K_E)} \left(\frac{s}{\omega_6} + 1 \right)}{\left(\frac{s}{\omega_4} + 1 \right) \left(\frac{s^2}{\omega_2^2} + \frac{2\zeta_2 s}{\omega_2} + 1 \right)} \quad (31)$$

Based on comparison, $G_{\text{pilot-o}}(s)$ has one more high-frequency first-order differential element than $G_{\text{pilot-c}}(s)$. However, the value of ω_7 is high; therefore, the effect of the first-order differential on the stability and rapidity of $G_{\text{pilot-o}}(s)$ is negligible. The Bode diagrams of the pilot valve subsystem are shown in Figure 7.

4.2.1 Stability, Rapidity, and Immunity of Pilot Valve Subsystem

As shown in Figure 7, $G_{\text{pilot-o}}(s)$ and $G_{\text{pilot-c}}(s)$ do not differ significantly within the operating frequency range of the relief valve unless the value of ω_a is sufficiently small that the delay of the first-order inertial element can significantly improve the stability of the pilot valve.

Similar to the stability analysis above, the rapidity of $G_{\text{pilot-o}}(s)$ or $G_{\text{pilot-c}}(s)$ does not differ significantly in the operating frequency range of the relief valve. However, if ω_a is sufficiently small, then the delay in the first-order inertial element may reduce the rapidity of the pilot valve.

As shown in Figure 7, $G_{\text{pilot-o}}(s)$ has one more high-frequency first-order differential element than $G_{\text{pilot-c}}(s)$, which implies that the immunity of $G_{\text{pilot-o}}(s)$ is lower than that of $G_{\text{pilot-c}}(s)$. Additionally, similar to the observation that ω_7 decreases with the size of orifice R_2 , the immunity of $G_{\text{pilot-o}}(s)$ decreases with the size of R_2 as well.

4.3 Dynamic Characteristics of Main Valve Subsystem

In the original model, the system transfer function of the main valve subsystem is expressed as follows:

$$G_{\text{main-o}}(s) = \frac{\frac{K_B(A_1 - K_D y_x)}{K_{m1}(K_A + K_C)} \left(\frac{s}{\omega_5} + 1 \right) \left(\frac{s}{\omega_7} + 1 \right)}{\left(\frac{s}{\omega_3} + 1 \right) \left[\left(\frac{s^2}{\omega_1^2} + \frac{2\zeta_1 s}{\omega_1} + 1 \right) \left(\frac{s}{\omega_7} + 1 \right) + \frac{s}{\omega_c} \right]}, \quad (32)$$

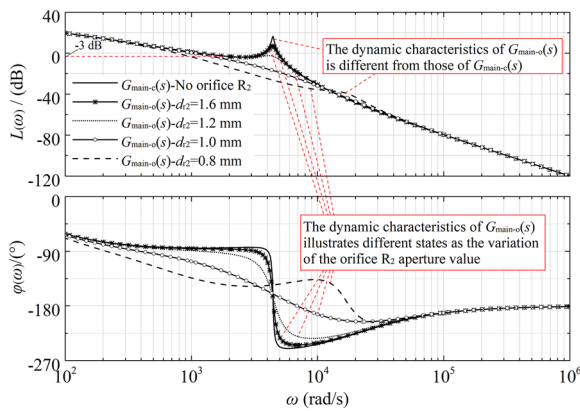


Figure 8 Bode diagrams of $G_{\text{main-o}}(s)$ and $G_{\text{main-c}}(s)$

$$\omega_c = \frac{G_r(k_1 + K_D p_{sx})}{A_1^2}, \tag{33}$$

where K_{m1} is the equivalent mechanical spring stiffness of the main valve, expressed as $K_{m1} = k_1 + K_D p_{sx}$; and ω_c is the equivalent break frequency produced by the dynamic pressure feedback orifice R_2 and main spring.

For the contrast model, the system transfer function of the main valve subsystem can be expressed as follows:

$$G_{\text{main-c}}(s) = \frac{K_B(A_1 - K_D y_x)}{K_{m1}(K_A + K_C)} \left(\frac{s}{\omega_5} + 1 \right) \left(\frac{s}{\omega_3} + 1 \right) \left(\frac{s^2}{\omega_1^2} + \frac{2\zeta_1 s}{\omega_1} + 1 \right). \tag{34}$$

Figure 8 shows the Bode diagrams of the main valve subsystem. As shown in Figure 8, the dynamic characteristics of $G_{\text{main-o}}(s)$ differ from those of $G_{\text{main-c}}(s)$. $G_{\text{main-o}}(s)$ is more stable than $G_{\text{main-c}}(s)$. By contrast, $G_{\text{main-c}}(s)$ is more rapid than $G_{\text{main-o}}(s)$. In addition, the stability of $G_{\text{main-o}}(s)$ illustrates different states, depending on the orifice R_2 aperture value. For further analysis, dimensional normalization was performed.

4.3.1 Normalization Analysis

By disregarding the minor effect of ζ_1 , the denominator term in Eq. (32) can be approximated using Eq. (35).

$$\left(\frac{s^3}{\omega_1^2 \omega_7} + \frac{s^2}{\omega_1^2} + \frac{s}{\omega_7} + \frac{s}{\omega_c} + 1 \right) \times \left(\frac{s}{\omega_3} + 1 \right). \tag{35}$$

Subsequently, Eq. (35) is converted into the product of two linear terms and a quadratic term, as shown in Eq. (36).

$$\left(\frac{s}{\omega_\alpha} + 1 \right) \left(\frac{s^2}{\omega_\beta^2} + \frac{2\zeta_\beta s}{\omega_\beta} + 1 \right) \times \left(\frac{s}{\omega_3} + 1 \right), \tag{36}$$

where ω_α is the break frequency of the first-order inertia element; and ω_β and ζ_β are the resonance frequency and damping ratio of the oscillation element, respectively. However, the values of ω_α , ω_β , and ζ_β cannot be obtained easily using a simple analytical method; hence, dimensional normalization was performed.

The assumptions introduced are as follows:

$$\omega_\alpha \omega_\beta^2 = \omega_7 \omega_1^2, \tag{37}$$

$$\frac{2\zeta_\beta}{\omega_\beta \omega_\alpha} + \frac{1}{\omega_\beta^2} = \frac{1}{\omega_1^2}, \tag{38}$$

$$\frac{1}{\omega_\alpha} + \frac{2\zeta_\beta}{\omega_\beta} = \frac{1}{\omega_7} + \frac{1}{\omega_c}. \tag{39}$$

Subsequently, the dimensionless transformation of Eqs. (37) to (39) yields

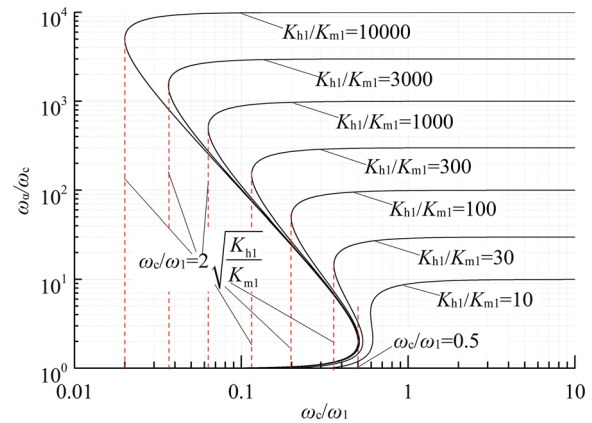


Figure 9 Real root normalization curve of Eq. (40)

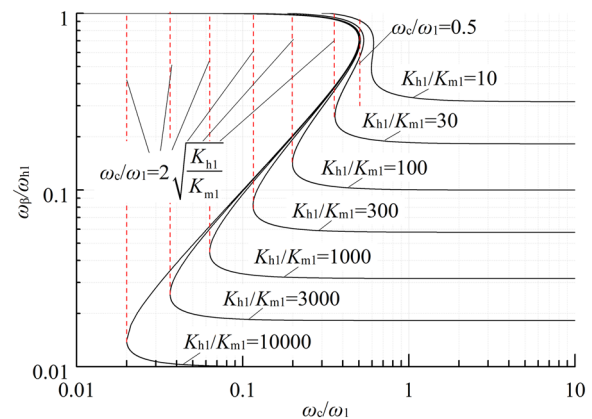


Figure 10 Real root normalization curve of Eq. (41)

$$\frac{\omega_c}{\omega_1} = \sqrt{\frac{\left(\frac{K_{h1}}{K_{m1}} + 1\right) \frac{\omega_\alpha}{\omega_{10}} - \frac{K_{h1}}{K_{m1}}}{\frac{K_{h1}}{K_{m1}} \left(\frac{\omega_\alpha}{\omega_{10}}\right)^2 - \left(\frac{\omega_\alpha}{\omega_{10}}\right)^3}}, \quad (40)$$

$$\frac{\omega_c}{\omega_1} = \sqrt{\frac{\left(\frac{K_{h1}}{K_{m1}} + 1\right) \left(\frac{\omega_\beta}{\omega_{h1}}\right)^4 - \frac{K_{h1}}{K_{m1}} \left(\frac{\omega_\beta}{\omega_{h1}}\right)^6}{\left(\frac{K_{h1}}{K_{m1}} \left(\frac{\omega_\beta}{\omega_{h1}}\right)^2 - 1\right)}}, \quad (41)$$

where K_{h1} is the equivalent spring stiffness of the liquid in chamber B, which is expressed as $K_{h1} = \frac{EA_1^2}{V_B}$. Because V_B is small, K_{h1} is large, and $K_{h1} \gg K_{m1}$, ω_{h1} is the natural frequency of the mass-spring vibration system formed by the main poppet and the liquid spring of chamber B, which is expressed as $\omega_{h1} = \frac{K_{h1}}{m_1}$.

The real root normalization curves of Eqs. (40) and (41) are shown in Figures 9 and 10, respectively. Because $K_{h1} \gg K_{m1}$ and $\frac{K_{h1}}{K_{m1}} \gg 1$, the stability of the main valve subsystem exhibits different states as the ratio of $\frac{\omega_c}{\omega_1}$ changes. Next, the following conditions are analyzed:

Condition I: If $\frac{\omega_c}{\omega_1} \geq 0.5$, then

$$\frac{\omega_\alpha}{\omega_c} = \frac{K_{h1}}{K_{m1}} = \frac{\omega_7}{\omega_c} \Rightarrow \omega_\alpha = \omega_7, \quad (42)$$

$$\omega_\beta = \omega_1 \sqrt{\frac{\omega_7}{\omega_\alpha}} \Rightarrow \omega_\beta = \omega_1, \quad (43)$$

$$\frac{1}{\omega_\alpha} + \frac{2\zeta_\beta}{\omega_\beta} = \frac{1}{\omega_7} + \frac{1}{\omega_c} \Rightarrow \zeta_\beta = \frac{\omega_1}{2\omega_c}. \quad (44)$$

In this case, Eq. (32) can be approximated as follows:

$$G_{\text{main-o}}(s) = \frac{\frac{K_B(A_1 - K_D \gamma_x)}{(K_A + K_C)K_{m1}} \left(\frac{s}{\omega_5} + 1\right)}{\left(\frac{s}{\omega_3} + 1\right) \left(\frac{s^2}{\omega_1^2} + \frac{1}{\omega_c} s + 1\right)}. \quad (45)$$

Condition II: If $\frac{\omega_c}{\omega_1} \leq 2\sqrt{\frac{K_{h1}}{K_{m1}}}$, then

$$\frac{\omega_\alpha}{\omega_c} \rightarrow 1 \Rightarrow \omega_\alpha = \omega_c, \quad (46)$$

$$\omega_\beta = \omega_1 \sqrt{\frac{\omega_7}{\omega_\alpha}} = \omega_1 \sqrt{\frac{\omega_7}{\omega_c}} = \omega_1 \sqrt{\frac{K_{h1}}{K_{m1}}} \Rightarrow \omega_\beta = \omega_{h1}, \quad (47)$$

$$\frac{2\zeta_\beta}{\omega_\beta} + \frac{1}{\omega_\alpha} = \frac{1}{\omega_7} + \frac{1}{\omega_c} \Rightarrow \zeta_\beta = \frac{\omega_{h1}}{2\omega_7}. \quad (48)$$

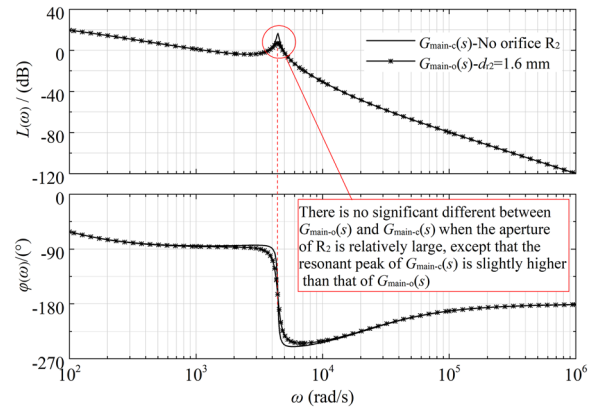


Figure 11 Bode diagrams of $G_{\text{main-o}}(s)$ and $G_{\text{main-c}}(s)$ under Condition I

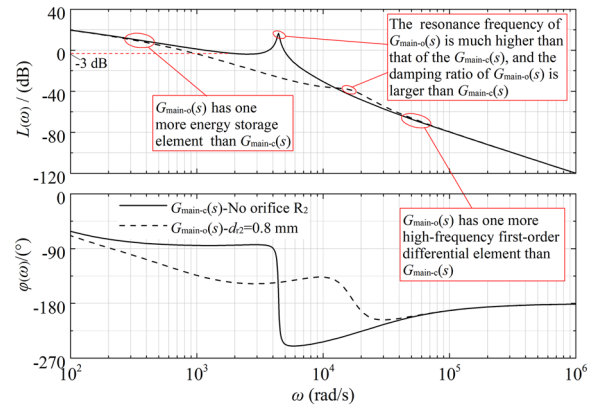


Figure 12 Bode diagrams of $G_{\text{main-o}}(s)$ and $G_{\text{main-c}}(s)$ under Condition II

In this case, Eq. (32) can be transformed into

$$G_{\text{main-o}}(s) = \frac{\frac{K_B(A_1 - K_D \gamma_x)}{(K_A + K_C)K_{m1}} \left(\frac{s}{\omega_5} + 1\right) \left(\frac{s}{\omega_7} + 1\right)}{\left(\frac{s}{\omega_3} + 1\right) \left(\frac{s^2}{\omega_{h1}^2} + \frac{1}{\omega_7} s + 1\right) \left(\frac{s}{\omega_c} + 1\right)}. \quad (49)$$

4.3.2 Stability, Rapidity, and Immunity of Main Valve Subsystem Under Condition I

Figure 11 shows the Bode diagrams of the main valve subsystem under Condition I. $G_{\text{main-o}}(s)$ and $G_{\text{main-c}}(s)$ did not differ significantly when the aperture of R_2 was relatively large, except for the resonant peak of $G_{\text{main-c}}(s)$, which was slightly higher than that of $G_{\text{main-o}}(s)$. Therefore, the damping ratio of $G_{\text{main-o}}(s)$ was slightly larger

than that of $G_{main-c}(s)$. In this case, the stability of the main valve subsystem might not improve significantly. Similarly, the rapidity and immunity of $G_{pilot-o}(s)$ and $G_{pilot-c}(s)$ did not differ significantly.

4.3.3 Stability, Rapidity, and Immunity of Main Valve Subsystem Under Condition II

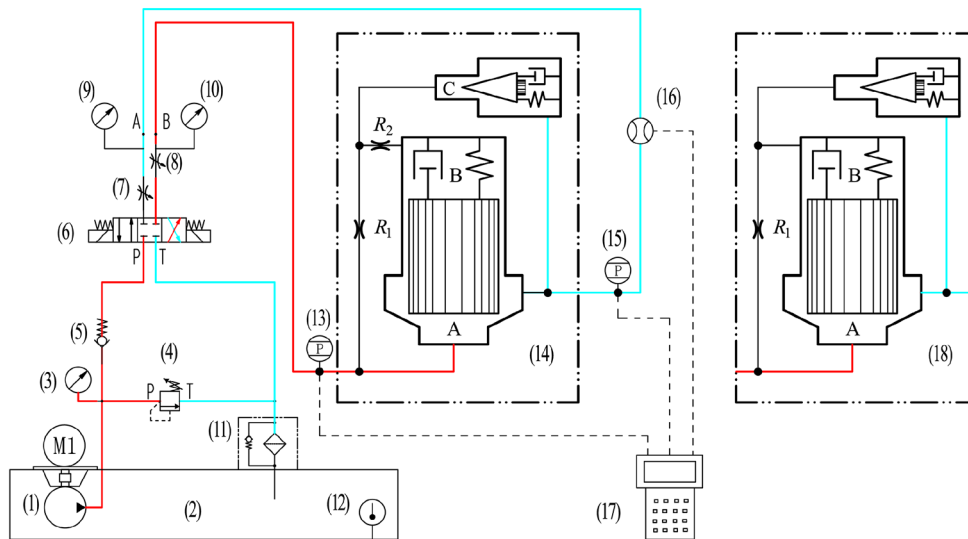
Figure 12 shows the Bode diagrams of the main valve subsystem under Condition II. Some differences were indicated between the $G_{main-o}(s)$ and $G_{main-c}(s)$. First, the resonance frequency of the oscillation element of $G_{main-o}(s)$ was much higher than that of $G_{main-c}(s)$. Second, the damping ratio of $G_{main-o}(s)$ was larger than that of $G_{main-c}(s)$. In addition, $G_{main-o}(s)$ had one more energy storage element (first-order inertial element) and one more high-frequency first-order differential element than $G_{main-c}(s)$. Similar to the previous discussion (Section 4.2), the value of ω_7 was high; therefore, the effect of the first-order differential on the stability and rapidity of $G_{main-o}(s)$ is negligible. As shown in Figure 12, if the break frequency (ω_c) of this additional energy-storage element is sufficiently small, then its delay can effectively improve the stability of the main valve. Contrary to the stability analysis

above, if ω_c is sufficiently small, then the delay of the energy-storage element may reduce the rapidity of the main valve. Notably, the immunity between $G_{main-o}(s)$ and $G_{main-c}(s)$ did not differ significantly because the delay of the energy-storage element effectively counteracted the lead of the first-order differential element. Therefore, $G_{main-o}(s)$ and $G_{main-c}(s)$ exhibited similar immunity.

Based on the analysis above, one can conclude that if the diameter of R_2 is sufficiently small, then a dynamic pressure feedback orifice designed between the main valve and pilot valve may effectively improve the local stability of the hydraulic pilot-operated relief valve, which contributes positively to the global stability of the entire valve. By contrast, the rapidity and immunity of the hydraulic pilot-operated relief valve may be weakened to some extent.

5 Simulation and Experimental Verification

The accuracy of the conclusions inferred the previous section was verified through numerical simulations and measurements.



(1) Fixed displacement pump; (2) Tank; (3) (9) (10) Pressure gauge; (4) Safety valve; (5) Check valve; (6) Solenoid directional valve; (7) (8) Throttle valve; (11) Filter; (12) Thermometer; (13) (15) Pressure sensor; (14) Original model; (16) Flowmeter; (17) Synchronous data acquisition instrument; (18) Contrast model

Figure 13 Schematic diagram of experimental system

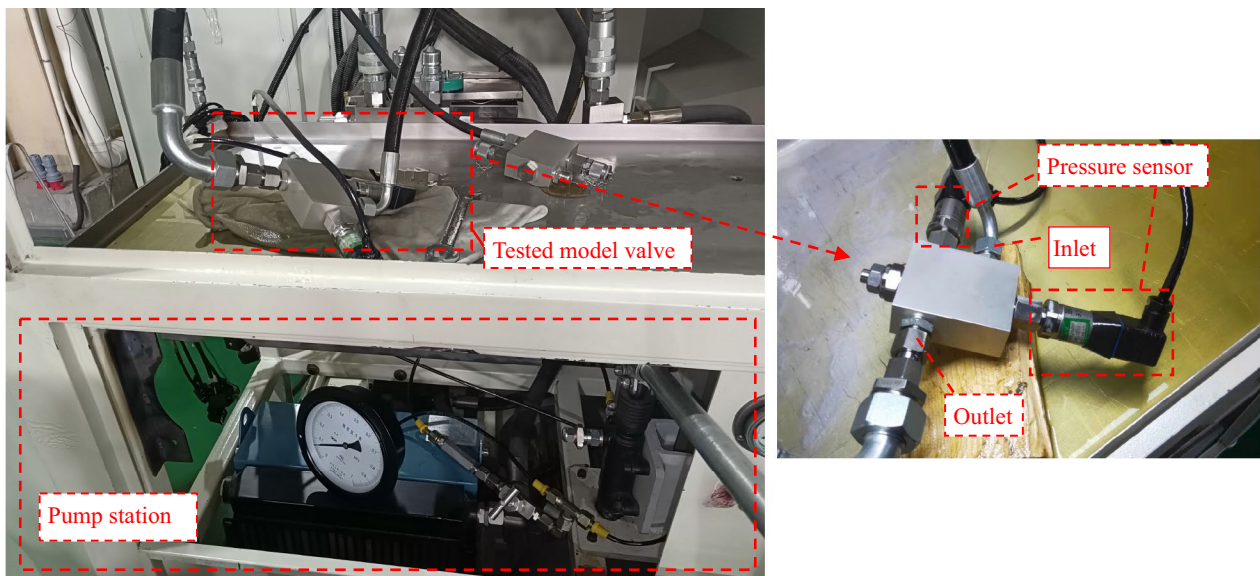


Figure 14 Experimental device and tested model valve

5.1 Numerical Simulation Model

A dynamic numerical simulation model of a relief valve was developed using MATLAB, and the nonlinearities were considered using appropriate Simulink blocks. For an accurate computation, solver “ode45” was used as the nonlinear system dynamics simulation mode, where the Runge–Kutta method was used with a fixed time step (1×10^{-6} s). The parameters used in the simulation were consistent with those listed in Table 3. The supply flow (Q_p-Q_t), which was gradually increased from 0 to 90 L/min, was used as the input signal, whereas the chamber A pressure p_s , pilot valve displacement x , and main valve displacement y were the output signals.

5.2 Experimental Model and Test Conditions

5.2.1 Experimental Device

Schematic diagrams of the experimental system and device are shown in Figures 13 and 14, respectively.

In the experimental system, RP-3 aerospace kerosene was used as the working medium, and a seamless steel pipe was used as the hydraulic pipeline. An external gear pump (1) driven by an electric motor was used to provide a constant flow of 140 L/min, and the pressure was measured using pressure sensors (13) and (15). The flow rate was measured using a flowmeter (16) (range: 16–160 L/min; accuracy: 0.5%FS). Data were acquired using a synchronous data acquisition instrument (17) at a sampling period of 1.0 ms. The parameters of the tested valve were consistent with those listed in Table 3.

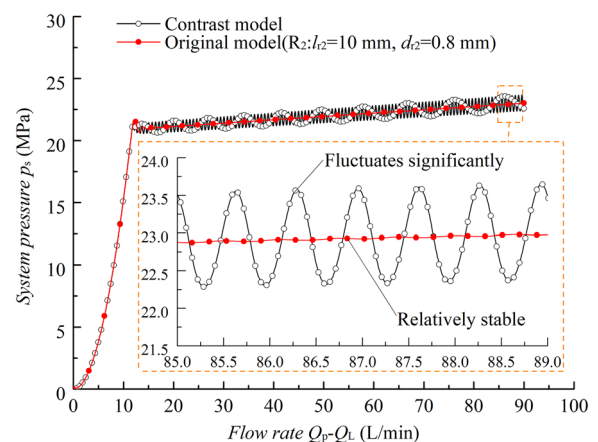


Figure 15 Pressure-flow diagrams of pilot-operated relief valve obtained via simulation

5.2.2 Experimental Scheme

The operational process stability of the relief valve was analyzed. The experimental scheme was formulated as follows: the inlet flow was gradually increased from 0 L/min to the rated flow (90 L/min) while the pressure in chamber A, p_s , was monitored. Subsequently, the pressure-flow characteristics of the relief valve were analyzed after all experimental data were obtained. During the experiment, the throttle valve (7) was opened to the maximum lift. Subsequently, the data acquisition device (17) was turned on, followed by the pump station, while the

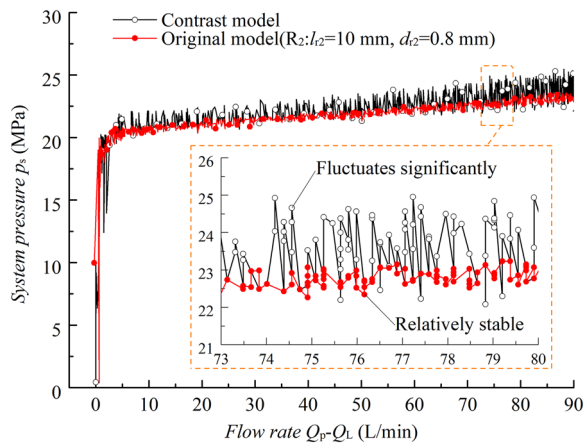


Figure 16 Pressure-flow diagrams of pilot-operated relief valve obtained via experiment

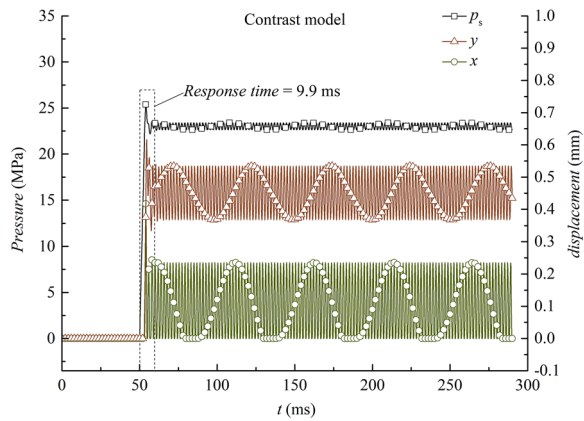


Figure 17 Pressure curves of contrast model

throttle valve (8) was adjusted to ensure that the flow rate increased gradually. Finally, the pump station was turned off, and data acquisition was terminated.

5.3 Simulation and Experimental Results

The pressure-flow characteristic curves of the original and contrast models obtained via simulation and experiment are shown in Figures 15 and 16, respectively. As shown, the simulation results agreed well with the experimental results.

As shown in Figures 15 and 16, during the entire process, the pressure-flow characteristic curves of the original model were smoother or more stable than those of the contrast model. By contrast, the pressure-flow

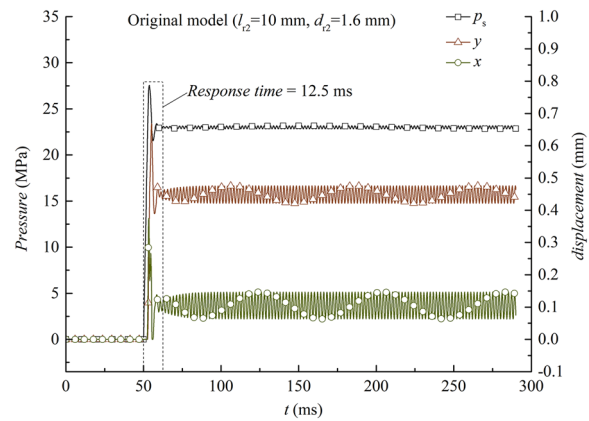


Figure 18 Pressure curves of original model ($d_{12} = 1.6$ mm)

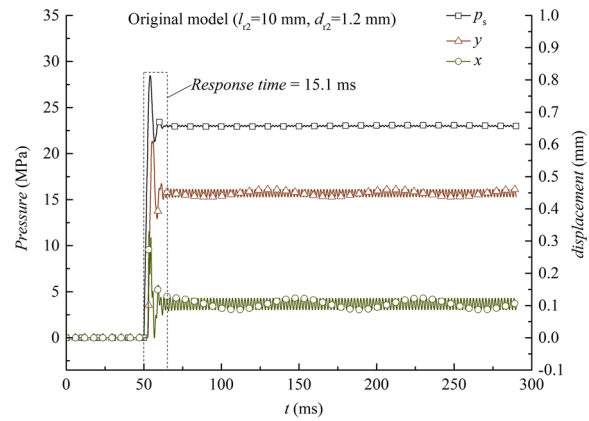


Figure 19 Pressure curves of original model ($d_{12} = 1.2$ mm)

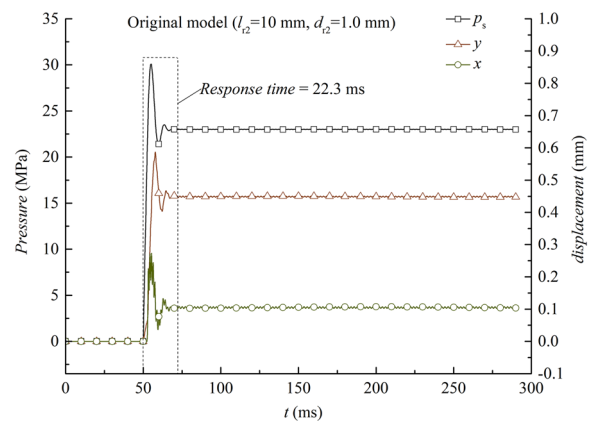


Figure 20 Pressure curves of original model ($d_{12} = 1.0$ mm)

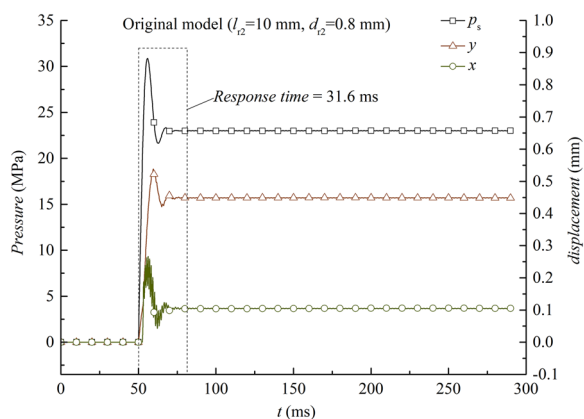


Figure 21 Pressure curves of original model ($d_2 = 0.8$ mm)

characteristic curves of the contrast model exhibited significant fluctuations. The experimental results show that the pressure fluctuation amplitude of the original model near the rated operating point was 0.39 MPa, which was approximately 1.6% of the rated pressure. However, the pressure fluctuation amplitude of the contrast model was approximately 1.64 MPa, which was approximately 6.6% of the rated pressure.

Combining the above with the results presented in Section 4, one can conclude that the contrast model valve is an unstable control system. Additionally, as shown in Figures 15 and 16, the flow-pressure characteristics of the valve do not change significantly after the addition of a damping orifice. Thus, designing an orifice between the main and pilot valves is beneficial for improving the stability of the hydraulic pilot-operated relief valve.

5.4 Effect on Valve Response Time

In general, stability and rapidity are contradictory. According to a previous study, an appropriate size of R_2 may enhance the stability of the relief valve. However, its effect on the valve response time remains unclear. Hence, the pressure response curves of the valve were obtained via numerical simulation, and the supply flow ($Q_p - Q_L$), which was stepped from 0 to 90 L/min at 50 ms, was used as the input signal, whereas chamber A pressure p_s , pilot valve displacement x , and main valve displacement y were specified as the output signals. Figures 17 and 21 present the simulation results for the relief valve response time.

As illustrated in Figures 17, 18, 19, 20 and 21, the response speed of the contrast model was high under step-signal excitation, and the pressure of the controlled chamber can reach the set value within approximately 9.9 ms (Figure 17). However, the original model with the dynamic pressure feedback orifice required at least

12.5 ms to reach the set value (Figure 18). More importantly, the response time of the relief valve can reach 31.6 ms (Figure 21) when the diameter of orifice R_2 does not exceed 0.8 mm for a steady pressure output.

The dynamic pressure feedback orifice results in a longer response time by the relief valve, although it improves the valve stability. Therefore, to satisfy the stability requirements, the diameter of R_2 should be set as large as possible.

6 Conclusions

In this study, the dynamic characteristics of a cartridge-type hydraulic pilot-operated relief valve were investigated through theoretical analysis and experiments, and the following conclusions were obtained:

- (1) For the case involving a larger dynamic pressure feedback orifice, the stability of the pilot-operated relief valve did not change substantially, except when its damping ratio was increased.
- (2) A small-diameter orifice resulted in high flow resistance, which was beneficial to the stability of the relief valve. In terms of control engineering, an energy-storage element with a lower break frequency was added to the pilot-operated relief valve system, which was beneficial for improving circuit stability. In addition, the oil inside the main spring chamber was equivalent to a liquid spring with an extraordinarily high stiffness, and the resonance frequency of the main valve subsystem increased significantly to a level far exceeding the regulating frequency of the relief valve.
- (3) The dynamic pressure feedback orifice resulted in a longer response time by the relief valve, although it improved the valve stability.
- (4) The simulation and experimental results showed that designing a dynamic pressure feedback orifice with an appropriate size between the main valve and pilot valve is beneficial to the stability of hydraulic pilot-operated relief valves.

Acknowledgements

The authors sincerely thanks to Engineer Jiali Guo and Engineer Sancheng Yu of the Shanghai Aerospace Control Technology Institute for their important assistance in the experiment.

Author Contributions

YY and JF were in charge of the whole trial; DW wrote the manuscript, and HJ assisted with the sampling and laboratory analyses. All the authors have read and approved the final version of the manuscript.

Authors' Information

Yaobao Yin born in 1965, is currently a professor at Tongji University, China. He received his Doctor of Engineering Degree in mechanical engineering from

Saitama University, Japan, in 1999, after obtaining M.S. degree in engineering from *Shanghai Jiao Tong University, China*, in 1991, and B.S. degree in mechanical engineering from *Shanghai Jiao Tong University, China*, in 1988. His research interests include basic theories of fluid power control, hydraulics and pneumatics in extreme environments, aircraft energy and servo mechanisms, high-speed pneumatic control, advanced energy and power control, and the basic theory of ocean wave power generation.

Dong Wang born in 1995, is currently a PhD candidate at *Tongji University, China*. He received his master degree from *Lanzhou University of Technology, China*, in 2019. His research interests include basic theory and application of hydraulic components.

Junyong Fu born in 1971, is currently an engineer at *Shanghai Aerospace Control Technology Institute, China*. He received his master degree from *Harbin Institute of Technology, China*, in 2005. His research interests include hydraulic transmission technology, fluid transmission, and fluid control.

Hong-chao Jian was born in 1989, is currently an engineer at *China North Vehicle Research Institute, China*. He received his PhD degree from the *Beijing Institute of Technology, China*, in 2018. His research interests include hydraulic transmission and vehicle engineering.

Funding

Supported by National Natural Science Foundation of China (Grant No. 52175059) and National Key Research and Development Program of China (Grant No. 2018YFB2001100).

Declarations

Competing Interests

The authors declare no competing financial interests.

Received: 16 March 2022 Revised: 12 July 2023 Accepted: 21 July 2023

Published online: 08 August 2023

References

- [1] Y B Yin. *Electro hydraulic control theory and its applications under extreme environment*. Oxford: Elsevier Inc, 2019: 273–281.
- [2] H F Vickers. Liquid relief valve. Patent US2043453, USA, 1931.
- [3] K Yonezawa. Flow-induced vibration of a steam control valve. *Journal of Fluids and Structures*, 2012, 35: 76–88.
- [4] S Hayashi. Instability of poppet valve circuit. *JSME International Journal*, 1995, 38(3): 357–366.
- [5] J Lei, J Tao, C Liu, et al. Flow model and dynamic characteristics of a direct spring loaded poppet relief valve. *Proceedings of the Institution of Mechanical Engineers, Part C: Journal of Mechanical Engineering Science*, 2018, 232(9): 1657–1664.
- [6] K Dasgupta, R Karmakar. Dynamic analysis of pilot operated pressure relief valve. *Simulation Modelling Practice and Theory*, 2001, 10: 35–49.
- [7] D N Johnston, K A Edge, M Brunelli. Impedance and stability characteristics of a relief valve. *Proceedings of the Institution of Mechanical Engineers Part I: Journal of Systems and Control Engineering*, 2002, 216(5): 371–382.
- [8] W Wei, H Jian, Q Yan, et al. Nonlinear modeling and stability analysis of a pilot-operated valve-control hydraulic system. *Advances in Mechanical Engineering*, 2018, 10(11): 1–8.
- [9] K Suzukia, E Urataa. Dynamic characteristics of a direct pressure sensing water hydraulic relief valve. *Proceedings of the 6th JFPS International Symposium on Fluid Power*, Tsukuba, Japan, November 7–10, 2005: 461–466.
- [10] Q F Ye, J P Chen. Dynamic analysis of a pilot-operated two-stage solenoid valve used in pneumatic system. *Simulation Modelling Practice and Theory*, 2009, 17: 794–816.
- [11] P Moussou. Instability of pressure relief valves in water pipes. *Proceedings of the ASME 2009 Pressure Vessels and Piping Division*. Prague, Czech Republic, July 26–30, 2009: 1–8.
- [12] X T Zhang, W L, Y M Zhang, et al. Experimental investigation and optimization design of multi-support pipeline system. *Chinese Journal of Mechanical Engineering*, 2021, 34(1): 10.
- [13] D Y Yi, L Lu, J Zou, et al. Interactions between poppet vibration and cavitation in relief valve. *Proceedings of the Institution of Mechanical Engineers Part C: Journal of Mechanical Engineering Science*, 2014, 203: 1989–1996.
- [14] W Min, H Wang, Z Zheng, et al. Visual experimental investigation on the stability of pressure regulating poppet valve. *Proceedings of the Institution of Mechanical Engineers Part C: Journal of Mechanical Engineering Science*, 2020, 234(4): 2329–2348.
- [15] K Kumagai. Investigation of poppet valve vibration with cavitation. *International Journal of Fluid Power*, 2016, 17(1): 5–24.
- [16] S Washio, A R Champneys. Nucleation and subsequent cavitation in a hydraulic oil poppet valve. *Mechanical Engineering Science*, 2016, 224: 947–958.
- [17] G Osama. Modeling of impact of the poppet element on its seat body in pressure relief valves. *Proceedings of the Institution of Mechanical Engineers Part I: Journal of Systems and Control Engineering*, 2020, 235(5): 703–720.
- [18] Y B Yin, J Y Yuan, J Y FU. Characteristics of two-stage relief valve with a series damping orifice in pilot valve front chamber. *Journal of Jilin University(Engineering and Technology Edition)*, 2017, 47(1): 129–136.
- [19] A Misra. Self-excited vibration of a control valve due to fluid-structure interaction. *Journal of Fluids and Structures*, 2002, 16(5): 649–665.
- [20] W J Ding. *Self-Excited Vibration: Theory, Paradigms, and Research Methods*. Beijing: Tsinghua University Press, 2011. (in Chinese)
- [21] Y J Gong, Z W Wang, J Xu, et al. Simulation and experiments study on water hydraulic pressure relief valve with pilot stage. *Chinese Journal of Mechanical Engineering*, 2010, 46(24): 136–142.
- [22] Q Zhong, H M Bao, Y B Li, et al. Investigation into the independent metering control performance of a twin spools valve with switching technology-controlled pilot stage. *Chinese Journal of Mechanical Engineering*, 2021, 34: 91.
- [23] Y H Liu, X Guan, P P Lu, et al. Simulation research on dynamic characteristics of hydraulic mount. *Chinese Journal of Mechanical Engineering*, 2021, 34(1): 49.
- [24] W Min, D Wang, Z Zheng. Visualization experiment of vibration and cavitation in poppet valve under low pressure condition. *Journal of Mechanical Engineering*, 2018, 54(50): 139–144.
- [25] H E Merrit. *Hydraulic control systems*. New York: John Willy & Sons, 1967.
- [26] R Shi, C L Wang, T He. Analysis of dynamic characteristics of pressure-regulating and pressure-limiting combined relief valve. *Physical Problems in Engineering*, 2021, 9: 1–13.

Submit your manuscript to a SpringerOpen[®] journal and benefit from:

- Convenient online submission
- Rigorous peer review
- Open access: articles freely available online
- High visibility within the field
- Retaining the copyright to your article

Submit your next manuscript at ► [springeropen.com](https://www.springeropen.com)